© 2017. Published by The Company of Biologists Ltd | Development (2017) 144, 4322-4327 doi:10.1242/dev.152124

RESEARCH REPORT

# Anisotropic shear stress patterns predict the orientation of convergent tissue movements in the embryonic heart

**Francesco Boselli[1,2,3], Emily Steed[1,2,3], Jonathan B. Freund[4] and Julien Vermot[1,2,3,*]**

## ABSTRACT

Myocardial contractility and blood flow provide essential mechanical cues for the morphogenesis of the heart. In general, endothelial cells change their migratory behavior in response to shear stress patterns, according to flow directionality. Here, we assessed the impact of shear stress patterns and flow directionality on the behavior of endocardial cells, the specialized endothelial cells of the heart. At the early stages of zebrafish heart valve formation, we show that endocardial cells are converging to the valve-forming area and that this behavior depends upon mechanical forces. Quantitative live imaging and mathematical modeling allow us to correlate this tissue convergence with the underlying flow forces. We predict that tissue convergence is associated with the direction of the mean wall shear stress and of the gradient of harmonic phase-averaged shear stresses, which surprisingly do not match the overall direction of the flow. This contrasts with the usual role of flow directionality in vascular development and suggests that the full spatial and temporal complexity of the wall shear stress should be taken into account when studying endothelial cell responses to flow *in vivo*.

**KEY WORDS: Fluid mechanics, Low Reynolds number, Red blood cells, *Danio rerio*, Morphogenesis, Photoconversion, Live imaging**

## INTRODUCTION

Shortly after the first heartbeat, a directional blood flow is established in the embryonic cardiovascular system. The resulting flow forces trigger specific endocardial cell responses that are essential to the orchestration of the morphogenetic events leading to heart development, including chamber ballooning, valve formation and trabeculation (Boselli et al., 2015; Collins and Stainier, 2016; Haack and Abdelilah-Seyfried, 2016). The tangential force generated by fluid flow at the cell surface can be characterized in terms of shear stress (Freund et al., 2012). The importance of shear stress and its temporal profile has been extensively discussed. For example, oscillatory shear stress has been shown to modulate the expression of *klf2a*, an important flow-responsive gene for heart chamber (Dietrich et al., 2014) and valve development (Vermot et al., 2009; Heckel et al., 2015; Steed et al., 2016a). It is not clear, however, how the pattern defined by spatial changes of shear stress and its dynamics could potentially impact endocardial cell behavior. A major role might be anticipated because microcirculation flow polarizes endothelial cells and orients their migration according to shear stress spatial gradients, with motion opposite to flow direction, as observed *in vitro* (Ostrowski et al., 2014) and *in vivo*, during vascular morphogenesis (Kochhan et al., 2013; Franco et al., 2015; Kwon et al., 2016).

To identify the morphogenetic response of endocardial cells (EdCs) to shear stress patterns *in vivo*, we examined the early events of the formation of the atrioventricular canal (AVC), which is the area between the forming atrium and ventricle, where the valve will develop and where strong local spatial and temporal gradients are expected.

## RESULTS AND DISCUSSION

### EdCs converge toward the AVC at the onset of valvulogenesis

In recent studies of the morphogenetic events leading to valve emanation, the number of EdCs in the AVC has been shown to increase significantly between 36 hpf and 48 hpf (Pestel et al., 2016; Steed et al., 2016b). To characterize the corresponding morphogenetic events, we took advantage of the *Tg(fli:kaede)* line, which expresses Kaede, a photosensitive protein that changes its emission spectrum after exposure to UV light (Ando et al., 2002), and is of great use to study cardiovascular morphogenesis in zebrafish (Chow and Vermot, 2017). We photoconverted the Kaede in the atrium and ventricle of hearts at 36 hpf (Fig. 1A) and imaged them at 36 hpf and 48 hpf (see Materials and Methods) (Fig. 1B,C). To capture the full three-dimensional process, we developed an image analysis approach based on segmentation and unfolding of the AVC region (Fig. 1D and Fig. 2; Materials and Methods), facilitated by the endocardium being a monolayer at this stage. In short, a reference system is introduced that defines each point on the AVC by its axial position along the AVC centerline and its azimuthal angle around that axis. The endocardium is then segmented on this parametric surface, with the image intensity projected onto it. This yields a two-dimensional image with each column and row corresponding to a well-defined azimuthal and arc-length position, respectively. The edges between the photoconverted and nonphotoconverted cells are then easily found (Fig. 1D; Materials and Methods). We measure the AVC lengths $L_{36}$ and $L_{48}$ at 36 hpf and 48 hpf, respectively, and compute the AVC shortening factor $(L_{48}-L_{36})/L_{36}$ as a function of the angular position. The shortening factor is averaged over the superior, inferior, interior and exterior regions of the AVC (Fig. 2A), which are defined based on the orientation of the elliptic cross-section of the AVC and its orientation within the embryo. For the wild type (Fig. 2B,C), we found that the distance between the photoconverted areas decreases in size and that the average AVC shortening factor varies from about −0.3 to −0.06

---

[1]Institut de Génétique et de Biologie Moléculaire et Cellulaire, 67404 Illkirch, France. [2]Centre National de la Recherche Scientifique, UMR7104, 67404 Illkirch, France. [3]Institut National de la Santé et de la Recherche Médicale, U964, 67404 Illkirch, France. [4]Mechanical Science & Engineering, University of Illinois at Urbana-Champaign, Urbana, IL 61801, USA.

*Author for correspondence (julien@igbmc.fr)

F.B., 0000-0002-6338-6321; E.S., 0000-0003-4742-2860; J.B.F., 0000-0002-7073-1365; J.V., 0000-0002-8924-732X

This is an Open Access article distributed under the terms of the Creative Commons Attribution License (http://creativecommons.org/licenses/by/3.0), which permits unrestricted use, distribution and reproduction in any medium provided that the original work is properly attributed.

**Received 16 March 2017; Accepted 31 August 2017**

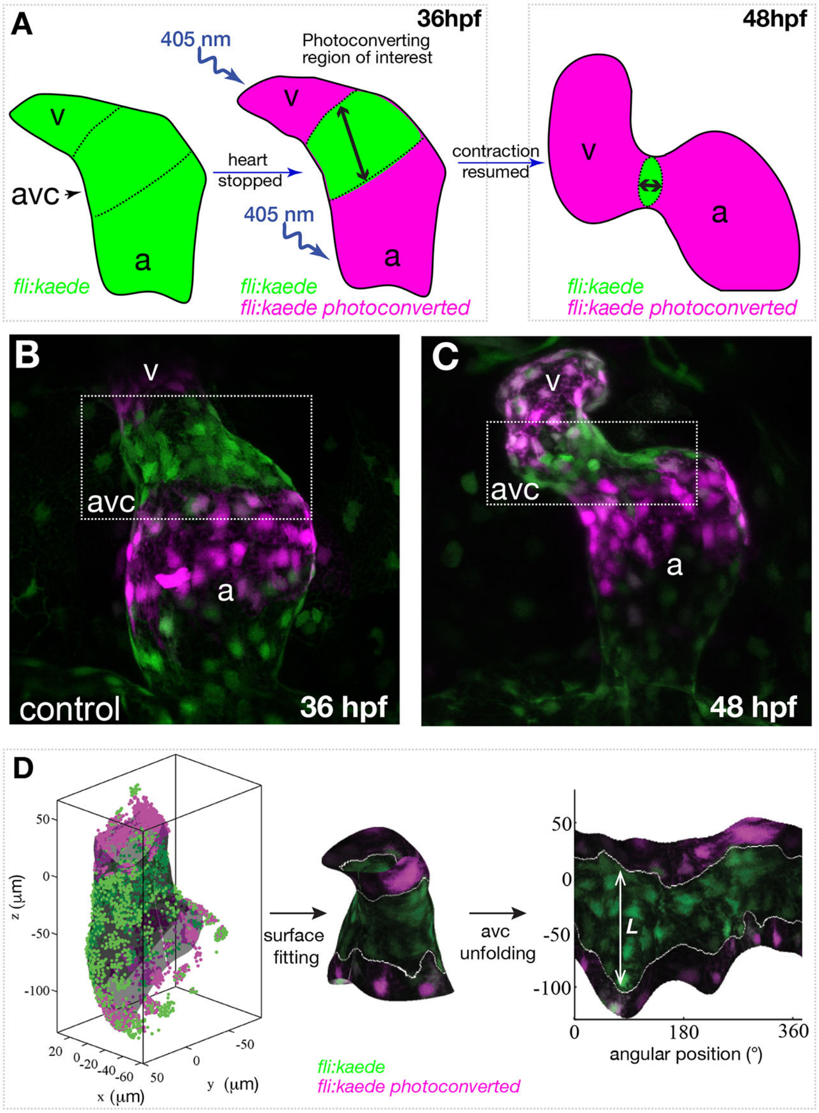
A
36hpf
405 nm
Photoconverting region of interest
v
avc
a
heart stopped
405 nm
v
a
fli:kaede
fli:kaede
fli:kaede photoconverted
contraction resumed
48hpf
v
a
fli:kaede
fli:kaede photoconverted
B
v
avc
a
control
36 hpf
C
v
avc
a
48 hpf
D
50
0
-50
-100
z (µm)
20
0
-20
-40
-60
x (µm)
-50
0
50
y (µm)
surface fitting
avc unfolding
fli:kaede
fli:kaede photoconverted
50
0
-50
-100
L
0
180
360
angular position (°)

**Fig. 1. Schematic of photoconversion experiments and of the three-dimensional analysis of early AVC morphogenesis.** (A) The atrium (a) and ventricle (v) of a 36 hpf *fli:kaede* heart are exposed to 405 nm UV light to photoconvert the genetically encoded Kaede protein from its green to red configuration. The same heart is imaged at 36 hpf and at 48 hpf to assay the movement of the photoconverted tissue. (B,C) Maximum intensity projection of a *fli:kaede* heart at 36 hpf and 48 hpf, respectively. (D) AVC segmentation and analysis: the endocardium of the AVC region is segmented with a parametric surface. The color intensity of the 3D dataset is projected on the parametric surface and the AVC is unfolded for 2D visualization and quantification of the length *L* of the photoconverted tissue.

(Fig. 2F). Considering that these cells will contribute to the AVC valve structure (Steed et al., 2016b; Pestel et al., 2016), these results suggest that the convergence of EdCs toward the AVC might be the first morphogenetic step of heart valve morphogenesis.

### EdC convergence toward the AVC is dependent upon mechanical forces

Early myocardial function has been shown to affect AVC development (Bartman et al., 2004). We thus assessed if this observed tissue movement is dependent on mechanical forces. Exploiting the well-documented ability of the zebrafish embryos to survive and develop without a functioning cardiovascular system until ∼5 dpf (Stainier et al., 1996), we first repeated the photoconversion experiment in *silent heart* (*sih*; *tnnt2a* – ZFIN) mutants, which lack heart contraction (Sehnert et al., 2002). Strikingly, the AVC shortening factor became positive, varying from ∼0.7 to 0.8 (Fig. 2D-F), indicating that the two photoconverted regions are in fact moving apart (Fig. 2F). We found in particular that the superior, inferior and exterior AVC shortening was different from the control ($P<0.05$). This suggests that cells require particular mechanical forces to cue convergence toward the center of the AVC (Fig. 2G).

### Red blood cells are not required for tissue convergence

As red blood cells (RBCs) have been suggested to provide mechanical cues to endothelial cells (Freund and Vermot, 2014), we next tested the influence of RBCs during tissue convergence. For this we studied *gata1* (*gata1a*) morphants, which almost totally inhibits hematopoiesis (Galloway et al., 2005). In these embryos, heart contractility is similar to that of controls (Vermot et al., 2009). We found that the AVC shortening factor varies from about −0.4 to −0.13 and was not significantly different from that of the controls, though with increased variability between embryos (Fig. 2F). Overall, these results suggest that RBCs are not essential to drive EdC convergence in the AVC, though this does not preclude some role in fine tuning the process.

### Fluid profiles in the AVC

The observed influence of mechanical forces on tissue convergence and the absence of a role for RBCs led us to assess the hemodynamics in more detail, in particular the directionality of the flow, generated between 33 hpf and 48 hpf. At these developmental stages, the beating heart works as a valveless pump, moving blood from the atrium to the ventricle through the AVC during diastole, and from the ventricle to the vascular system during systole. On average, the

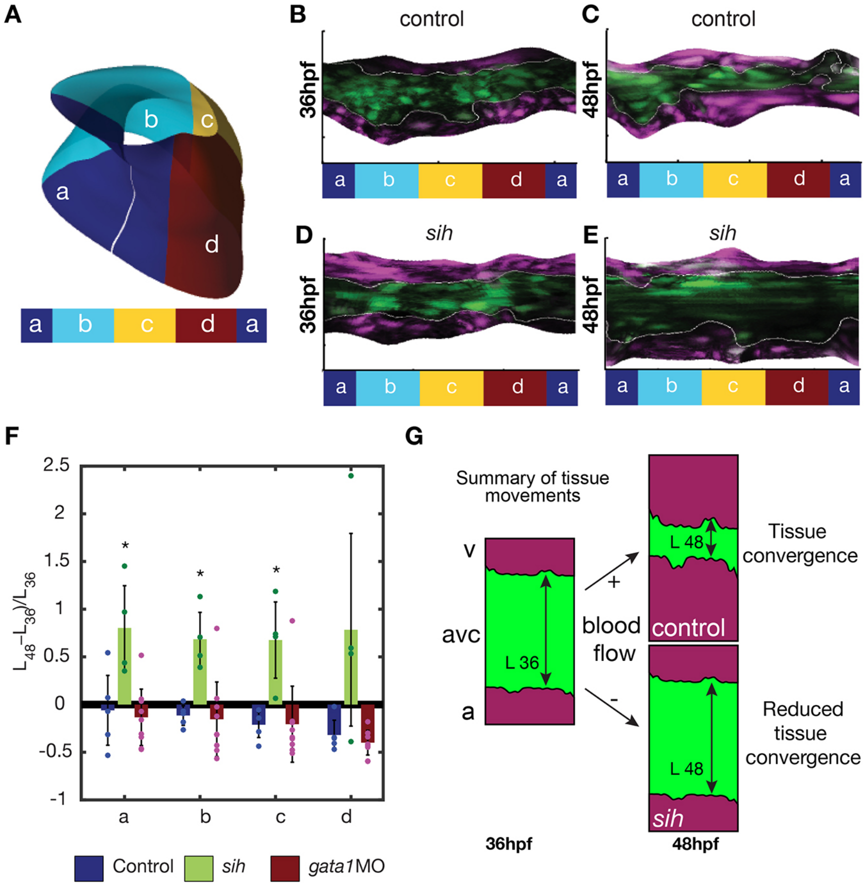

**Fig. 2. Tissue convergence (AVC shortening) is flow dependent.** (A) Schematic showing the compartmentalization into superior (a), inferior (c), exterior (b) and interior (d) regions of the AVC. (B-E) Unfolded visualization of the *fli:kaede* (control) (B,C) and *sih;fli:kaede* AVC endocardium (D,E) at 36 hpf (B,D) and 48 hpf (C,E). (F) The shortening index ($L_{48}$–$L_{36}$)/$L_{36}$ of the AVC between 36 hpf and 48 hpf in control (*n*=5), *sih* (*n*=4) and *gata1* (*n*=9) morphants is averaged on the a,b,c,d regions. $L_{48}$ and $L_{36}$ are the AVC length *L* at 48 hpf and 36 hpf, respectively. Data are mean±s.d. Statistical significance was determined by unpaired Student's *t*-test; $^*0.01<P<0.05$. (G) Schematic of flow-dependent tissue convergence.

flow is unidirectional between the atrium and the ventricle, but is oscillatory, and at times reversing in the AVC (Scherz et al., 2008; Vermot et al., 2009). Video recordings taken at a series of time points between 33 hpf and 48 hpf show this flow profile in the beating hearts of *Tg(gata1:dsred;fli:kaede)* embryos, in which RBCs and endocardial wall are labeled (Fig. S1A-F). These show that transiently reversing flows are almost continuous in the AVC between 36 hpf and 48 hpf. This is clearly visible when RBCs are advected from the ventricle to the atrium through the AVC in between the ventricular and atrial contractions (Fig. S1A-F). Similar results were previously discussed for *gata1* morphants (Vermot et al., 2009; Heckel et al., 2015). Thus, AVC development has a remarkable distinction from microcirculation morphogenesis, where endothelial cells tend to move away from oscillatory flows and upstream toward high shear stress regions with well-defined flow directionality in the vascular network (Kochhan et al., 2013; Franco et al., 2015; Kwon et al., 2016). Such cell behavior seems incompatible with the observed EdCs converging into the AVC, which suggests that the mechanical cue underlying EdCs behavior is more likely to be associated with the shear stress pattern generated by the oscillatory flow and its local reversals rather than that of the mean flow direction.

## Modeling hemodynamic wall shear stress and RBC contribution

To understand the shear stress patterns at work in the beating heart, we developed a model for blood flow in a simplified beating heart tube. It includes explicit RBCs that are expected to contribute to the shear stress pattern in space and time at the scales of the embryonic heart (Freund and Vermot, 2014; Fung, 1993; Boselli et al., 2015). The geometry is two-dimensional and includes key features of this flow: moving wall and flexible cells, with each RBC modeled as an elastic shell that can deform in response to shear flows and is fully coupled with the flow mechanics (see Materials and Methods). This simple RBC model is sufficient to reproduce key features of confined RBC channel flows, including the near-wall cell-free layers (Freund, 2007), rheological behaviors (Bryngelson and Freund, 2016a) and stability characteristics (Bryngelson and Freund, 2016b). The overall heart is represented as a linear tube with walls that move harmonically with amplitude and phase at each location based on the live imaging data. Our computational approach exploits the low Reynolds number of the zebrafish heart, ~0.1, which means that inertia is negligible (Santhanakrishnan and Miller, 2011). Despite its obvious simplifications (see Materials and Methods), our model reproduces the key *in vivo* behavior: It is a valveless pump that forces an on-average unidirectional blood flow from the atrium inflow to the ventricle outflow. The flow is particularly unsteady, combining both pulsatile and oscillatory flow, matching that observed during AVC maturation. There are also reversals, with RBCs flowing backwards and forwards through the AVC (Fig. S1G-I, Movie 1). This model therefore recapitulates the main features of the embryonic heart and allows us to characterize the complex wall shear stress patterns arising under such flow conditions.

## Shear stress consists of periodic and nonperiodic components

To gain insight into the physical stimuli generated by the flow EdCs experience in the developing heart, we undertook a comprehensive analysis of the shear stress obtained with our simulations. The shear stress evaluated at the wall, which corresponds to the shear stress

EdCs experience, $\tau(t)$, is a particularly unsteady signal because the endocardial walls are extremely dynamic in the embryonic heart. The wall shear stress signal is seen as the combination of two periodic components and one nonperiodic component: a constant signal, harmonic signals and nonperiodic oscillatory signals, respectively. The constant signal is the time average of the shear stress, $\tau_0$. The harmonic signals are sine functions and the frequency of each harmonic is a multiple of the heart beat frequency, which is the fundamental frequency of the system, $f_1$. The amplitude of each harmonic signal can be computed via a standard Fourier analysis of the phase average of the shear stress signal over multiple heart beats. The average shear stress plus the harmonic oscillations represent the periodic component of the shear stress, $\bar{\tau}$. The nonperiodic component, $\tilde{\tau}(t)$, is associated with the chaotic dynamics of the RBCs (Fig. 3A-F), which is different at each heart beat, and is quantified as the root mean square (rtm) of the deviation of the shear stress signal from its periodic component: $\tilde{\tau}(t) = rms(\tau(t) - \bar{\tau}(t))$ (Table S1).

To simplify our analysis, we considered these components separately. We first considered the periodic components of the wall shear stress. The time-average shear stress $\tau_0$ is largest on the boundaries of the AVC. It is positive (atrium to ventricle direction) at the ventricular side and negative (ventricle to atrium direction) at the atrial side of the AVC (Fig. 3H-K), which means that it is not linked to the atrium-to-ventricle mean direction of blood flow. We next considered the fundamental harmonic signal $\tau_1$ (oscillating with the heart beat frequency $f_1$) and found that it makes the largest contribution to the wall shear stress in the AVC (Fig. 3I-M). Its maximum is at the center of the AVC. This confirms previous computations with a simpler model without RBCs (Heckel et al., 2015; Boselli and Vermot, 2016). Higher frequency harmonics (for example $\tau_2$, $\tau_3$,…, oscillating with frequency $2f_1$, $3f_1$,…) have a similar profile though lower amplitude (Fig. S2). Finally, we considered the nonperiodic component ($\tilde{\tau}$) and found it is maximum at the AVC region and with peak values comparable to those of the time average $\tau_0$ (Fig. 3N,P), resembling the profile of $\tau_1$. These results suggest that the pattern of each shear stress component represents a physical landmark cells could specifically sense in the AVC.

### Impact of RBCs on the pattern of the shear stress components

We next addressed the contribution of RBCs on the components of the shear stress distribution in order to better characterize the *gata1* morphants devoid of RBCs, and to assess the robustness of our results with respect to the stiffness and shape of the RBC model. The amplitude of the fundamental harmonic signal $\tau_1$ and the other harmonics increase almost linearly with the number of RBCs, $n_{rbc}$, and therefore preferentially in the AVC. By contrast, the pattern of the average shear stress $\tau_0$ is more sensitive to $n_{rbc}$, and increases unevenly with $n_{rbc}$ at the ventricular side of the AVC (Fig. 3H-K). This effect depends on the uneven distribution of the RBCs and the formation of RBC-depleted regions (Fig. S1K; Fig. 3G). In our simple model, depleted regions can be observed, for example, close to the upper (as shown) atrial wall at the AVC inflow (Fig. S1K), where the wall shear stress increases slower with the number of

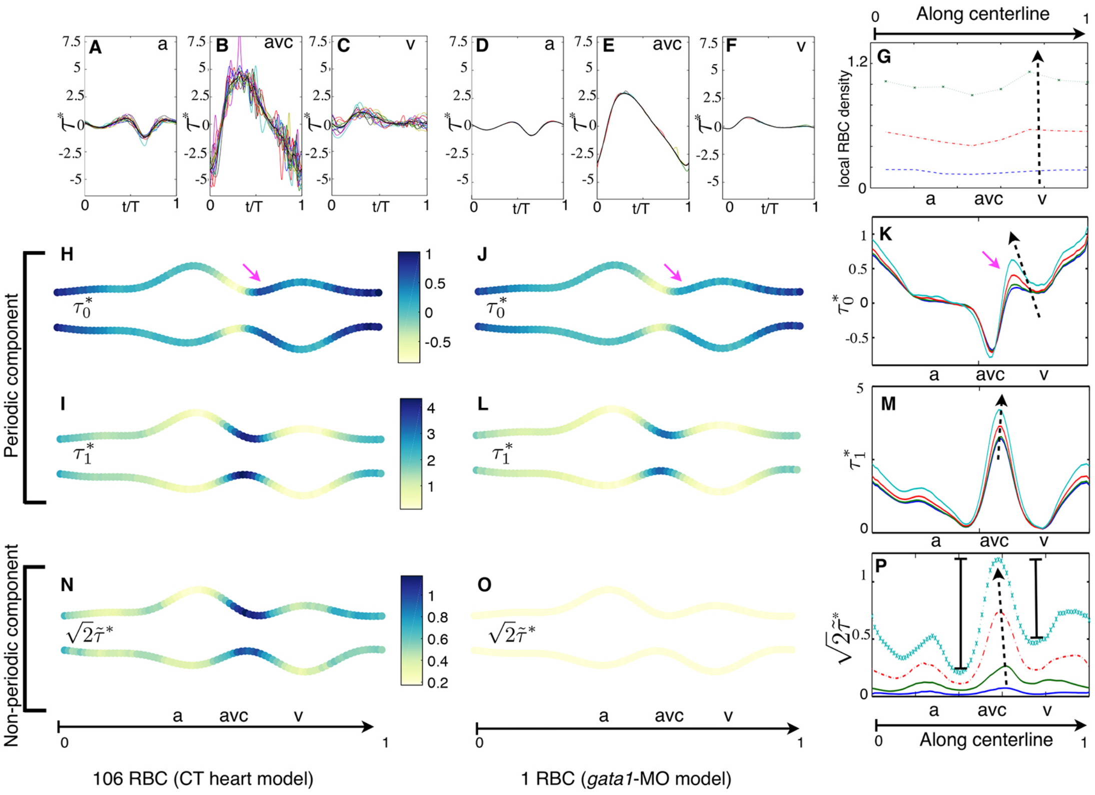

**Fig. 3. Shear stress pattern during tissue convergence.** (A-F) Wall shear stress $\tau$ as a function of time at a point on (A,D) the atrial side (a), (B,E) the center (avc) and (C,F) the ventricular side (v) of the AVC. Different colors correspond to different heart cycles. Their phase-average (black line) is the periodic-component $\bar{\tau}$ of $\tau$. (H-K) Time average $\tau_0$ and (I-M) fundamental harmonic amplitude $\tau_1$ of the periodic component $\bar{\tau}$ along the heart wall. (N-P) Nonperiodic oscillation $\tilde{\tau}$ of the shear stress (scaled by $\sqrt{2}$ for consistency). A-C,H,I,N and D-F,J,L,O correspond to simulations with 106 and 1 RBCs (red blood cells), respectively. (G) RBC concentration along the heart. The results in K, M and P are for the upper wall and for different numbers of RBCs: $n_p$=1, 17, 54,106 (dashed arrows point to larger values of $n_p$). Pink arrows in H-K point out the uneven contribution of $n_p$ to $\tau_0$. Asterisks denote results that are normalized by the space average of $\int_t f_1|\tau|dt$.

RBCs (Fig. 3K). Live imaging of *Tg(gata1:dsred)* also shows RBC clustering and RBC-depleted regions (Fig. S1L,M), suggesting that a nonintuitive contribution of RBCs to wall shear stress patterning must be expected in the beating heart as well. However, the pattern of both $\tau_0$ and $\tau_1$, including the direction of the former, do not change qualitatively, demonstrating that the results for the periodic components hold independently of the number of RBCs used in the simulations.

Not surprisingly, we found that the nonperiodic component $\tilde{\tau}$ goes to zero for $n_{rbc}=0$ (Fig. 3O). As for $\tau_0$, RBC clustering alters the pattern of $\tilde{\tau}$ such that nonperiodic oscillations are less important in RBC-depleted regions (Fig. 3P).

Finally, while the stiffness and shape of the RBCs impact wall shear stress, with stiffer RBCs leading to stronger values of all the shear stress components (Fig. S3), the patterns of each component of the wall shear stress remain qualitatively the same. Thus, our results are independent of the physical parameters describing the RBC model.

### The computed periodic components of wall shear stress predict tissue convergence orientation

We next dissected the biological importance of each shear stress component as a mechanical cue for tissue convergence in the AVC by comparing the results obtained experimentally with those from our simulations. As discussed, tissue convergence in the AVC is also observed in the hearts of *gata1* morphants (Fig. 2F), where the nonperiodic contribution of the RBCs ($\tilde{\tau}$) is negligible, such that $\tilde{\tau}$ does not appear to be a necessary mechanical cue for this specific morphogenetic event.

By contrast, the major features of the periodic components of the shears stress are conserved in the wild types and *gata1* morphants and are potential cues for tissue convergence. We thus conclude that the periodic components are the best predictor of EdC convergence in the AVC observed *in vivo*, but not flow direction or the nonperiodic component.

### Mechanistic model and conclusion

We considered the early morphogenetic events between 36 hpf to 48 hpf that ultimately lead to AVC maturation and valve formation. Using live imaging and three-dimensional image analysis, we showed that EdCs converge into the AVC and this process depends upon mechanical forces. Mathematical modeling allowed us to analyze the shear stress patterns associated with the reversing, oscillatory flow in the AVC. Though previous studies have illuminated the fluid dynamics of the developing heart (Jamison et al., 2013; Lee et al., 2013; Heckel et al., 2015; Miller, 2011; Taber et al., 2007; Midgett et al., 2015; Boselli and Vermot, 2016), this model allows us to account for the cellular character of blood in the heart at these stages. The highly unsteady, oscillatory, reversing flow, together with the dynamic boundaries of the endocardial walls give the flow and shear stress patterns in the AVC a complexity exceeding that of the rest of the circulation (Anton et al., 2013). The direction of the time average shear stress, $\tau_0$, and the gradient of the fundamental harmonics amplitude, $\nabla\tau_1$, does not match with the mean direction of blood flow (Fig. 4). Instead, they point away from and toward the AVC center, respectively (Fig. 4). Thus EdCs move in the direction of higher oscillation amplitudes of the phase average wall shear stress and opposite to the direction of the time average $\tau_0$, thus converging in the AVC (Fig. 4).

This study leaves us with several unresolved questions. First, the cellular mechanisms leading to tissue convergence in the AVC remain an open issue, but we speculate that cell intercalation (Tada and Heisenberg, 2012), cell proliferation and/or cell migration (Eder et al., 2016; LeGoff and Lecuit, 2016) are involved. Second, future work using realistic three-dimensional geometries will be necessary to study potential azimuthal patterns involved in nontrivial force generation. Third, beside shear stress, additional mechanical stimuli might be generated at the cellular scale, such as the strain associated with cell deformation and myocardial contractility. Thus, it will be important to assess the respective impact of myocardial contractility, the strain and the shear stress exerted on the endocardial cells behaviors. It is to note that our model does not suggest any obvious pattern of normal stress (perpendicular to the endocardium) that could establish a convergence zone in the AVC. However, we do not have a constitutive model of the heart wall and its coupling with the vascular system and thus we cannot be conclusive on the role of tissue strain and normal forces.

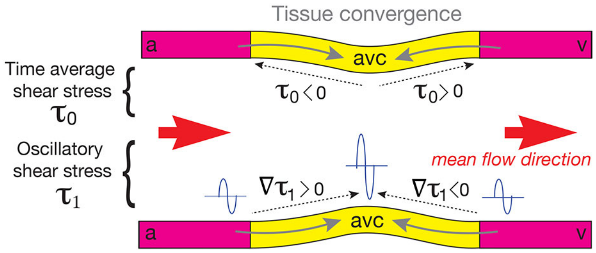

**Fig. 4. Schematic of the AVC illustrating the relationship between the directions of the converging movements of EdCs, mean shear stress, gradient of the amplitude of the fundamental harmonic and average flow.** Gray arrows indicate the directions of the converging movements of the EdCs, dotted arrows (upper wall) indicate the direction of the mean shear stress $\tau_0$, dotted arrows (lower wall) indicate the direction of the gradient of the amplitude of the fundamental harmonic $\nabla\tau_1$, and orange arrows indicate the average flow direction. Tissue moves toward higher values of the amplitude of the fundamental harmonic $\tau_1$ (illustrated with sine waves), which is in the same direction as its gradient $\nabla\tau_1$ and against the direction of the time average shear stress $\tau_0$. This does not match with the direction of the average blood flow (orange arrows), which is from atrium (a) to ventricle (v) along the heart. The center of the AVC is in yellow and the atrial and ventricular sides are in magenta. This configuration is a direct consequence of the typical reversing flow observed at 36-48 hpf in the AVC.

Overall, our results suggest that the reversing, oscillatory flow in the AVC leads to particular shear stress patterns that can establish a convergence zone in the AVC though the average blood flow is unidirectional (Fig. 4). Thus, shear stress patterns rather than flow directionality are potential determinants of the flow dependent morphogenetic events leading to valve development.

## MATERIALS AND METHODS

### Zebrafish husbandry, embryo treatments and morpholinos

Animal experiments were approved by the Animal Experimentation Committee of the Institutional Review Board of the IGBMC. Zebrafish lines used in this study were *Tg(fli1a:gal4FUBS; UAS:kaede)* (Herwig et al., 2011), *silent heart* (*sih*) (Sehnert et al., 2002), and *Tg(gata1:dsRed)* (Traver et al., 2003). For specific experiments, a morpholino for *gata1* (*gata1* MO) was injected into the yolk at the one-cell stage as described previously (Galloway et al., 2005; Vermot et al., 2009). All animals were incubated at 28.5°C for 5 h before treatment with 1-phenyl-2-thiourea (PTU) (Sigma-Aldrich) to prevent pigment formation.

### Photoconversion and *in vivo* imaging

Photoconversion experiments and live imaging were performed using the FRAP module of a confocal microscope (Steed et al., 2016b). *Tg(fli1a:gal4FUBS; UAS:kaede)* hearts were exposed to 405 nm light to convert the Kaede protein to its red form. A standard *z*-stack of the photoconverted heart was then acquired at both 36 hpf and 48 hpf. See Supplementary Materials and Methods for details.

### Three-dimensional analysis and statistical analysis

The three-dimensional analysis of the photoconverted cells was performed using a newly developed approach implemented in MATLAB. The AVC region was segmented, fitted with a parametric surface, and unfolded for two-dimensional visualization and quantification of the shortening factor $(L_{48}-L_{36})/L_{36}$, with $L_{36}$ and $L_{48}$ the length of the nonphotoconverted AVC region at 36 hpf and 48 hpf, respectively. See supplementary Materials and Methods for details. We repeated the experiment twice, and analyzed $n$=5 controls, $n$=4 *sih* mutants and $n$=9 *gata1* morphants. The statistical significance of the differences between the mean values calculated for control and perturbed flow conditions was determined by unpaired Student's *t*-tests. See supplementary Materials and Methods for details.

### Computational modeling

Fluid dynamic simulations were based on a new research code based on efficient boundary integral methods (Freund, 2007) for the solution of Stokes flow equations. This exploits the low Reynolds number, Re, of the zebrafish heart (Re<1), where inertia is almost negligible and the linearization underling the Stokes flow equations is appropriate. See supplementary Materials and Methods for details.

#### Acknowledgements

We thank the Vermot laboratory for discussions and thoughtful comments on the manuscript. We also thank the IGBMC fish facility (S. Geschier and S. Gredler) and the IGBMC imaging center, in particular B. Gurchenkov, E. Guiot and D. Hentsch.

#### Competing interests

The authors declare no competing or financial interests.

#### Author contributions

Conceptualization: J.V., F.B.; Methodology: F.B., E.S., J.B.F.; Software: F.B., J.B.F.; Formal analysis: J.B.F., F.B.; Data curation: E.S., F.B.; Writing - original draft: J.V., F.B., E.S., J.B.F.; Writing - review & editing: J.V., F.B., E.S., J.B.F.; Visualization: F.B., E.S.; Supervision: J.V., J.B.F.; Project administration: J.V.; Funding acquisition: J.V.

#### Funding

This work was supported by the European Research Council [682938 – EVALVE], Fondation pour la Recherche Médicale [DEQ29553], Agence Nationale de la Recherche [ANR-15-CE13-0015-01, ANR-10-IDEX-0002-02, ANR-12-ISV2-0001-01 and ANR-10-LABX-0030-INRT] and the European Molecular Biology Organization Young Investigator Program. Deposited in PMC for immediate release.

#### Supplementary information

Supplementary information available online at
http://dev.biologists.org/lookup/doi/10.1242/dev.152124.supplemental

#### References

**Ando, R., Hama, H., Yamamoto-Hino, M., Mizuno, H. and Miyawaki, A.** (2002). An optical marker based on the UV-induced green-to-red photoconversion of a fluorescent protein. *Proc. Natl. Acad. Sci. USA* **99**, 12651-12656.

**Anton, H., Harlepp, S., Ramspacher, C., Wu, D., Monduc, F., Bhat, S., Liebling, M., Paoletti, C., Charvin, G., Freund, J. B. et al.** (2013). Pulse propagation by a capacitive mechanism drives embryonic blood flow. *Development* **140**, 4426-4434.

**Bartman, T., Walsh, E. C., Wen, K.-K., McKane, M., Ren, J., Alexander, J., Rubenstein, P. A. and Stainier, D. Y. R.** (2004). Early myocardial function affects endocardial cushion development in zebrafish. *PLoS Biol.* **2**, E129.

**Boselli, F. and Vermot, J.** (2016). Live imaging and modeling for shear stress quantification in the embryonic zebrafish heart. *Methods* **94**, 129-134.

**Boselli, F., Freund, J. B. and Vermot, J.** (2015). Blood flow mechanics in cardiovascular development. *Cell. Mol. Life Sci.* **72**, 2545-2559.

**Bryngelson, S. H. and Freund, J. B.** (2016a). Buckling and its effect on the confined flow of a model capsule suspension. *Rheol. Acta* **55**, 451-464.

**Bryngelson, S. H. and Freund, J. B.** (2016b). Capsule-train stability. *Phys. Rev. Fluids* **1**, 033201.

**Chow, R. and Vermot, J.** (2017). The rise of photoresponsive protein technologies applications in vivo: a spotlight on zebrafish developmental and cell biology. *F1000Res.* **6(F1000 Faculty Rev)**, 459.

**Collins, M. M. and Stainier, D. Y. R.** (2016). Chapter twenty-five-organ function as a modulator of organ formation: lessons from zebrafish. *Curr. Top. Dev. Biol.* **117**, 417-433.

**Dietrich, A.-C., Lombardo, V. A. and Abdelilah-Seyfried, S.** (2014). Blood flow and bmp signaling control endocardial chamber morphogenesis. *Dev. Cell* **30**, 367-377.

**Eder, D., Aegerter, C. and Basler, K.** (2016). Forces controlling organ growth and size. *Mech. Dev.* **144**, 53-61.

**Franco, C. A., Jones, M. L., Bernabeu, M. O., Geudens, I., Mathivet, T., Rosa, A., Lopes, F. M., Lima, A. P., Ragab, A., Collins, R. T. et al.** (2015). Dynamic endothelial cell rearrangements drive developmental vessel regression. *PLoS Biol.* **13**, e1002125.

**Freund, J. B.** (2007). Leukocyte margination in a model microvessel. *Phys. Fluids* **19**, 023301.

**Freund, J. B. and Vermot, J.** (2014). The wall-stress footprint of blood cells flowing in microvessels. *Biophys. J.* **106**, 752-762.

**Freund, J. B., Goetz, J. G., Hill, K. L. and Vermot, J.** (2012). Fluid flows and forces in development: functions, features and biophysical principles. *Development* **139**, 1229-1245.

**Fung, Y. C.** (1993). *Biomechanics: Mechanical Properties of Living Tissues*. New York, NY: Springer.

**Galloway, J. L., Wingert, R. A., Thisse, C., Thisse, B. and Zon, L. I.** (2005). Loss of gata1 but not gata2 converts erythropoiesis to myelopoiesis in zebrafish embryos. *Dev. Cell* **8**, 109-116.

**Haack, T. and Abdelilah-Seyfried, S.** (2016). The force within: endocardial development, mechanotransduction and signalling during cardiac morphogenesis. *Development* **143**, 373-386.

**Heckel, E., Boselli, F., Roth, S., Krudewig, A., Belting, H.-G., Charvin, G. and Vermot, J.** (2015). Oscillatory flow modulates mechanosensitive *klf2a* expression through *trpv4* and *trpp2* during heart valve development. *Curr. Biol.* **25**, 1354-1361.

**Herwig, L., Blum, Y., Krudewig, A., Ellertsdottir, E., Lenard, A., Belting, H.-G. and Affolter, M.** (2011). Distinct cellular mechanisms of blood vessel fusion in the zebrafish embryo. *Curr. Biol.* **21**, 1942-1948.

**Jamison, R. A., Samarage, C. R., Bryson-Richardson, R. J. and Fouras, A.** (2013). *In vivo* wall shear measurements within the developing Zebrafish heart. *PLoS ONE* **8**, e75722.

**Kochhan, E., Lenard, A., Ellertsdottir, E., Herwig, L., Affolter, M., Belting, H.-G. and Siekmann, A. F.** (2013). Blood flow changes coincide with cellular rearrangements during blood vessel pruning in Zebrafish embryos. *PLoS ONE* **8**, e75060.

**Kwon, H.-B., Wang, S., Helker, C. S., Rasouli, S. J., Maischein, H.-M., Offermanns, S., Herzog, W. and Stainier, D. Y.** (2016). In vivo modulation of endothelial polarization by Apelin receptor signalling. *Nat. Commun.* **7**, 11805.

**Lee, J., Moghadam, M. E., Kung, E., Cao, H., Beebe, T., Miller, Y., Roman, B. L., Lien, C.-L., Chi, N. C., Marsden, A. L. et al.** (2013). Moving domain computational fluid dynamics to interface with an embryonic model of cardiac morphogenesis. *PLoS ONE* **8**, e72924.

**LeGoff, L. and Lecuit, T.** (2016). Mechanical forces and growth in animal tissues. *Cold Spring Harb. Perspect Biol.* **8**, a019232.

**Midgett, M., Chivukula, V. K., Dorn, C., Wallace, S. and Rugonyi, S.** (2015). Blood flow through the embryonic heart outflow tract during cardiac looping in HH13–HH18 chicken embryos. *J. R. Soc. Interface* **12**, 20150652.

**Miller, L. A.** (2011). Fluid dynamics of ventricular filling in the embryonic heart. *Cell Biochem. Biophys.* **61**, 33-45.

**Ostrowski, M. A., Huang, N. F., Walker, T. W., Verwijlen, T., Poplawski, C., Khoo, A. S., Cooke, J. P., Fuller, G. G. and Dunn, A. R.** (2014). Microvascular endothelial cells migrate upstream and align against the shear stress field created by impinging flow. *Biophys. J.* **106**, 366-374.

**Pestel, J., Ramadass, R., Gauvrit, S., Helker, C., Herzog, W. and Stainier, D. Y. R.** (2016). Realtime 3D visualization of cellular rearrangements during cardiac valve formation. *Development* **143**, 2217-2227.

**Santhanakrishnan, A. and Miller, L. A.** (2011). Fluid dynamics of heart development. *Cell Biochem. Biophys.* **61**, 1-22.

**Scherz, P. J., Huisken, J., Sahai-Hernandez, P. and Stainier, D. Y. R.** (2008). High-speed imaging of developing heart valves reveals interplay of morphogenesis and function. *Development* **135**, 1179-1187.

**Sehnert, A. J., Huq, A., Weinstein, B. M., Walker, C., Fishman, M. and Stainier, D. Y. R.** (2002). Cardiac troponin T is essential in sarcomere assembly and cardiac contractility. *Nat. Genet.* **31**, 106-110.

**Stainier, D. Y., Fouquet, B., Chen, J.-N., Warren, K. S., Weinstein, B. M., Meiler, S. E., Mohideen, M., Neuhauss, S. C., Solnica-Krezel, L., Schier, A. F. et al.** (1996). Mutations affecting the formation and function of the cardiovascular system in the zebrafish embryo. *Development* **123**, 285-292.

**Steed, E., Boselli, F. and Vermot, J.** (2016a). Hemodynamics driven cardiac valve morphogenesis. *Biochim. Biophys. Acta* **1863**, 1760-1766.

**Steed, E., Faggianelli, N., Roth, S., Ramspacher, C., Concordet, J.-P. and Vermot, J.** (2016b). *klf2a* couples mechanotransduction and zebrafish valve morphogenesis through fibronectin synthesis. *Nat. Commun.* **7**, 11646.

**Taber, L. A., Zhang, J. and Perucchio, R.** (2007). Computational model for the transition from peristaltic to pulsatile flow in the embryonic heart tube. *J. Biomech. Eng.* **129**, 441-449.

**Tada, M. and Heisenberg, C.-P.** (2012). Convergent extension: using collective cell migration and cell intercalation to shape embryos. *Development* **139**, 3897-3904.

**Traver, D., Paw, B. H., Poss, K. D., Penberthy, W. T., Lin, S. and Zon, L. I.** (2003). Transplantation and in vivo imaging of multilineage engraftment in zebrafish bloodless mutants. *Nat. Immunol.* **4**, 1238-1246.

**Vermot, J., Forouhar, A. S., Liebling, M., Wu, D., Plummer, D., Gharib, M. and Fraser, S. E.** (2009). Reversing blood flows act through *klf2a* to ensure normal valvulogenesis in the developing heart. *PLoS Biol.* **7**, e1000246.

# Supplementary Material

## Materials and Methods

### Materials and Experimental Methods

**Photoconversion and in vivo imaging** Photoconversion was performed using the FRAP module of a confocal microscope (TCS SP8, Leica microsystems) equipped with Leica HCX IRAPO L, x25, NA0.95 water immersion objective, as described previously (Steed et al., 2016).

*Tg(fli1a:Gal4FF; UAS:Kaede)* embryos were mounted in 0.7% low melting-point agarose (Sigma Aldrich) supplemented with 50 mM BDM to inhibit heart contraction at about 36hpf. Regions in the ventricle and the atrium were exposed to 405 nm light by applying 35 bleach pulses (35 ms each; 25% laser power). This converted the kaede protein to its red form. A standard z-stack of the photoconverted heart at 36hpf was then acquired, with 2 $\mu$m between the z-sections.

Embryos were then carefully dissected from the agarose, placed in fish water for 5-10 min until heart contraction resumed and then put at 28.5 °C to develop individually under standard conditions until 48hpf. A second z-stack was then acquired at 48hpf under the same conditions as for the 36hpf acquisitions.

In order to analyze tissue movement under perturbed flow conditions, the same experiment was repeated for the *Tg(fli1a:Gal4FF; UAS:Kaede)* injected with *gata1* MO, and for crosses of *sih* and *Tg(fli1a:Gal4FF; UAS:Kaede)*.

Live imaging of the beating heart was performed using light sheet microscopy (TCS SP8 DLS, Leica Microsystem) for the flow analysis between 36 and 48 hpf (Fig. S1) and confocal microscopy (TCS sp8, Leica microsystems) for the AVC shortening analysis. z-stacks of the beating hearts were synchronized post acquisition as previously described (Liebling et al., 2006).

**AVC unfolding, quantification of the AVC shortening, and statistical analysis** The three-dimensional movement of the photoconverted cells within each heart was analyzed using a newly developed approach.

The following steps are implemented in Matlab scripts.

- Step 1: Points on the endocardium are identified by intensity thresholding of the acquired images and plotted in three dimensions. Points on the atrium and the ventricle are erased interactively using the erase command of Matlab to isolate points representing the narrowest and most straight part of the AVC. These points are selected and fitted with a cylinder as described previously (McMahon et al., 2008). A reference system can then be introduced with the axis of the cylinder as z-axis and the center of mass of the AVC points as origin. The endocardial points are reoriented such that the points on the ventricle have a positive $z$- (axial) position. The heart points are then rotated around the z-axis with this strategy: The AVC points are projected on the x-y plane and fitted with an ellipse. The endocardial points are then rotated around the z-axis to bring the major ellipse axis parallel to the y-axis and such that the internal side of the AVC (with respect to the embryo) points has positive y-values. At this point, the angular position of cells in the AVC is defined consistently for all the hearts.

- Step 2: The three-dimensional dataset is cut by planes obtained by rotating the half-plane $\{y=0,\ x>0\}$ in the $z$-direction. The intensity of the neighboring pixels are projected on these planes and the endothelium traced with a line of points ordered with increasing arc-length from the atrium to the ventricular side of the AVC. These points are then interpolated by a three dimensional spline (spline toolbox, matlab). Each point on the resulting surface have a well defined angular position and the tissue length between two points at the same angular position is computed as the archlenght on the surface between the two points. This is different than the length of a linear segment between two points because the endocardium is curved.

- Step 3: The intensity of the neighboring pixels are projected on the parametric surface. This gives a two-dimensional image with each column corresponding to the line on the surface at a given angle. This is equivalent to unfold the AVC into a two-dimensional image.

- Step 4: The unfolded AVC can then be segmented in two-dimensions with standard tools to find the edges of the non-photoconverted AVC and the AVC length $L$ as a function of the angular position.

The same analysis was repeated at 36 and 48 hpf for each heart considered, and the AVC shrinking factor was computed as $(L_{48} - L_{36})/L_{36}$ as a function of the angular position and averaged over the inferior, superior, internal and external regions of the AVC (Fig. 2), which are defined consistently based on the orientation of the elliptic cross-section of the AVC and its orientation within the embryo.

The statistical significance of the differences between the mean values calculated for control and perturbed flow conditions was determined by unpaired Student's *t*-tests and computed with the `ttest2` function of the Matlab Statistical Toolbox, without assuming equal variances. Shown standard deviations were computed as corrected sample standard deviations using the `std` Matlab function.

## Computational Methods

**Heart dynamics and anatomy** We exploit the viscous regime of the zebrafish heart, where the Reynolds number is reported to vary from 0.017 at 26hpf to 0.342 at 4.5 days post fertilization (Santhanakrishnan and Miller, 2011). Therefore we neglect inertia effects, though they might alter details at 4.5dpf, as well as the overall curvature of the heart which will not alter flow substantively at so low of Reynolds numbers. In two dimensions, the dynamics of a point on the wall is simply defined as: $y(x, t) = d_0 + A \sin(t/f_1 2\pi + \theta_1)$ for both the upper and lower walls, where we truncate the Fourier expansion of $d(t)$ to the heart beat frequency $f_1$. The time average radius $d_0$ and the oscillation amplitude $A$ and the beating frequency $f_1$ were previously extracted from live imaging of 48hpf zebrafish hearts as described previously (Boselli and Vermot, 2016). Previous works showed how two-dimensional models can well predict typical shear stress in the heart of zebrafish embryos (Lee et al., 2013; Boselli and Vermot, 2016), which is the focus of this work. Therefore, despite the fact that an accurate description of some hemodynamic cues, including pressure, would require a three-dimensional model of the heart and of the hydrodynamic load represented by the vascular system, we will simplify the system and limit our analysis to two dimensions.

**RBC model** The membrane of each red blood cell (RBC) is modelled as an elastic shell of tension modulus $T$ and bending modulus $M$. The interior of the cell is molded as a fluid with the same viscosity as the plasma surrounding the cell. The flow of the plasma and of the cytosol are treated as Stokesian such that the flow velocity $u_i$ can be expressed by the boundary integral

$$u_i(\mathbf{x}, \mathbf{t}) = \frac{1}{4\pi\mu} \int_\Omega S_{ij}(\mathbf{y} - \mathbf{x})\, \Delta\sigma_j(\mathbf{y})\, ds(\mathbf{y}), \tag{1}$$

where $S_{ij}$ is the Stokeslet tensor, $s$ is the arc-length position of a point $\mathbf{x}(s)$ on the membrane, and $\Delta\sigma_j$ is the traction of the membrane on the fluid. For the cell membrane, the traction is given by the relation:

$$\Delta\sigma_i = \frac{\partial\tau}{\partial s} t_i + \frac{\partial}{\partial s}\left(\frac{\partial b}{\partial s} n_i\right), \tag{2}$$

with $\tau$ the membrane tension,

$$\tau = T\left(\frac{ds}{ds_0} - 1\right), \tag{3}$$

and $b$ the bending moment,

$$b = M\left(C(s) - C_0\right), \tag{4}$$

with $C$ the curvature and $C_0$ a constant initial curvature that cancels out in (2). The coordinate $s_0$ in Eqations (3) and (4) is the referential arch-length position of a point on the cell membrane in an hypothetic stress-free configuration. In practice, the stress-free shape of the RBCs does not need to be defined. It is sufficient to set the perimeter $l_0$ of the stress-free membrane and the area $r_0^2\pi$ of each of our two-dimensional RBCs such that $l_0 \neq 2\pi r_0$. Starting from an arbitrary initial configuration (here a sphere of perimeter $2\pi r_0$), the RBC will assume a configuration that minimize the elastic energy of the membrane. The time required by this process scales like the relaxation time of the red blood cell $\tau_{rlx} = r_0\mu/T$, and its ratio with the convective time scale $\tau_U = r_0/U$ gives a non dimensional index of the elasticity of the red blood cells (Freund, 2007). The main simulations were set-up such that $\tau_{rlx}/\tau_U = 0.16$, $r_0^2 T/M = 12.5$ and $l_0/(2\pi r_0) = 1.6\pi$. Simulations presented in Fig. S3, where repeated for $l_0/(2\pi r_0) = 1.2\pi$, $\tau_{rlx}/\tau_U = 0.1$, and $\tau_{rlx}/\tau_U = 0.32$, which, in the order, correspond to rounder, stiffer and softer red blood cells. The research code is available upon request.

**Wall model** The heart walls dynamics is obtained by imposing the wall traction

$$\Delta\sigma_i^w = -k_w(x_i - x_i^w). \tag{5}$$

which is equivalent to link each point on the wall to their desired location $\mathbf{x}^w$ by a virtual spring of stiffness $k_w$, which was kept constant and such that $k_w r_0^2/T = 1.5$ in the main simulations.

The flow velocity due to the wall traction can be expressed by the same boundary internal formulation (1) used for the cell membrane, but with $\Delta\sigma_i^w$ instead of $\Delta\sigma_i^m$. As for the RBCs, the number of points necessary to describe the shape of the wall is smaller than that required to compute the integrals along the wall. Only these control points are carried on during time integration. The extra collocation points for the space integrals are then obtained by Fourier interpolation, which exploits the periodicity of the boundary.

**Time integration** A point $\mathbf{x} = \{x_i\}$ on the cell membrane or on the wall moves then according to

$$\frac{\partial x_i}{\partial t} = u_i(\mathbf{x}, t), \tag{6}$$

where $u_i$ now is the sum of the contribution of all the cell membranes and the walls in the model system. Time integration is performed by a second order Runge-Kutta scheme. The time step $dt$ was set such that $dt * f_1 = 5 \cdot 10^{-5}$.

**Numerical discretization** The boundary integral (1) is computed by a quadrature around the periodic membranes (cells and walls). The quadrature can be computed on a uniform grid by discretizing the membrane with $N_a$ points uniformly spaced in $s_0$ and by expressing the Cartesian $\mathbf{x}(\mathbf{s_0})$ and the archlength $s(s_0)$ coordinates as a function of $s_0$:

$$u_i^m = \frac{1}{4\pi\mu} \sum_{n=1}^{N_a} S_{ij}(\mathbf{x}^n - \mathbf{x}^m)\, \Delta\sigma_j^n \, \frac{ds}{ds_0}|^n \Delta s_0 \tag{7}$$
$$\text{for} \quad m = 1 \dots N;$$

where $N_a$ is the number of points on the cell membrane and wall used for the quadrature and $N = N^m + N^w + N^v$ is the number of evaluation points, which is the sum of $N^m$ collocation points used to represent the cell membrane, $N^w$ wall points, and $N^v$ points where to evaluate $u_i$ for post processing or simply for visualization.

The numerical discretization, including the PME method employed to speed up the evaluation of (7), is described in details in (Freund, 2007). Starting from the results in (Freund, 2007), the collocation points on the membrane of each RBCs was set to $128$, and to $800$ on the wall.

**Computation of the shear stress** The integral boundary methods extend the flow domain over the whole space such that flow is also computed outside the actual domain of interest. Therefore, the wall shear stress at the endocardial interface is computed as $\tau_w = \sigma_i^w t_i^w + \tau_{out}$, where $t_i^w$ is the unit tangent vector to the wall and $\tau_{out}$ is the wall shear stress due to the flow outside the heart model. This is computed as $\tau_{out} = (u_i|_d t_i^w - u_i|_w t_i^w)/d$ where d is chosen to minimize $\sigma_i^w t_i^w - \tau_{out} - \tau_{in}$ without RBCs. $\tau_{in}$ is not computed directly to avoid the finite difference kernel to overlap with an RBC passing very close to the wall.The research code is available upon request.

## References and Notes

Boselli, F. and Vermot, J. (2016). Live imaging and modeling for shear stress quantification in the embryonic zebrafish heart. Methods *94*, 129–134.

Freund, J. B. (2007). Leukocyte margination in a model microvessel. Phys. Fluids *19*, 023301.

Lee, J., Moghadam, M. E., Kung, E., Cao, H., Beebe, T., Miller, Y., Roman, B. L., Lien, C.-L., Chi, N. C., Marsden, A. L. and Hsiai, T. K. (2013). Moving Domain Computational Fluid Dynamics to Interface with an Embryonic Model of Cardiac Morphogenesis. PLoS ONE *8*, e72924.

Liebling, M., Vermot, J., Forouhar, A. S., Gharib, M., Dickinson, M. E. and Fraser, S. E. (2006). Nonuniform temporal alignment of slice sequences for four-dimensional imaging of cyclically deforming embryonic structures. In 3rd IEEE International Symposium on Biomedical Imaging: Nano to Macro, 2006. pp. 1156–1159,.

McMahon, A., Supatto, W., Fraser, S. E. and Stathopoulos, A. (2008). Dynamic analyses of Drosophila gastrulation provide insights into collective cell migration. Science *322*, 1546–50.

Santhanakrishnan, A. and Miller, L. A. (2011). Fluid Dynamics of Heart Development. Cell Biochemistry and Biophysics *61*, 1–22.

Steed, E., Faggianelli, N., Roth, S., Ramspacher, C., Concordet, J.-P. and Vermot, J. (2016). klf2a couples mechanotransduction and zebrafish valve morphogenesis through fibronectin synthesis. Nat Commun *7*, 11646.

# Supplementary figures and movies

Supplements include one movie: Movie 1; there supplementary figures: Fig. S1, S2, 3; and Table S1.

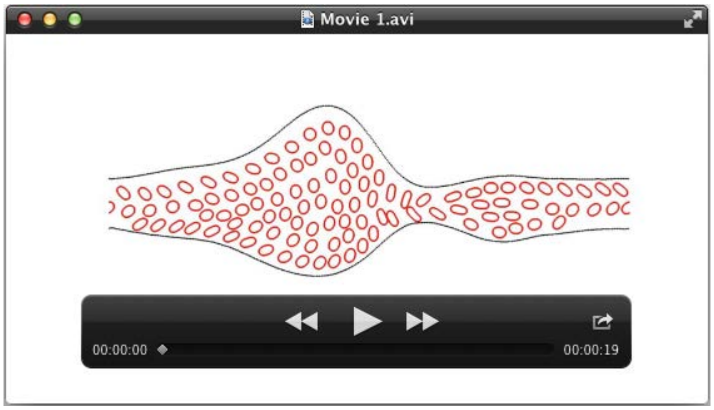

Movie 1: Related to Fig. S1G-I and 3. This movie illustrates the dynamics of 106 red blood cells (red) and of the walls (black) in the proposed computational model of the embryonic heart.

| symbol | definition |
|---|---|
| $\tau$ | wall shear stress |
| $\bar{\tau}$ | phase average of $\tau$ |
| $\tau_0$ | time average of $\tau$ |
| $\tau_1$ | fundamental harmonic component of $\tau$, oscillating with the same frequency as the heart $f_1$ |
| $\tau_n$ | harmonic component of $\tau$ oscillating at frequency $f_n$ |
| $\tilde{\tau}$ | root mean square ($rms$) amplitude of non periodic oscillations associated to the chaotic flow of red blood cells |

Table S1: Brief definition of the symbols used in the analysis of the wall shear stress.

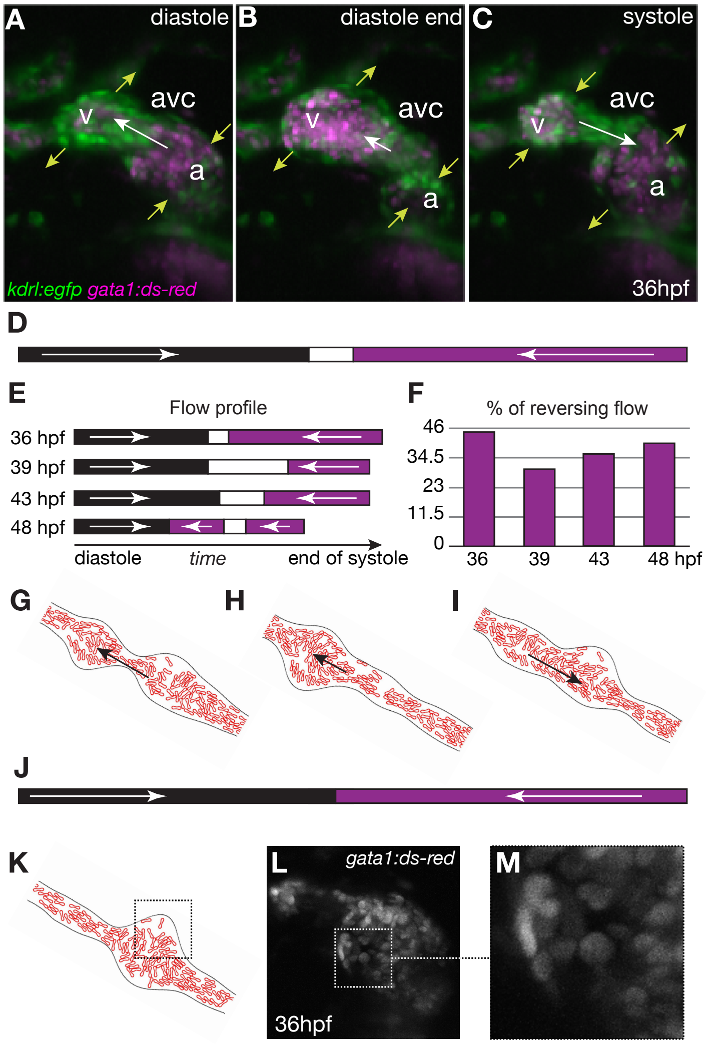
A
diastole
B
diastole end
C
systole
avc
v
a
kdrl:egfp gata1:ds-red
36hpf
D
E
Flow profile
36 hpf
39 hpf
43 hpf
48 hpf
diastole
time
end of systole
F
% of reversing flow
46
34.5
23
11.5
0
36
39
43
48 hpf
G
H
I
J
K
L
gata1:ds-red
36hpf
M

Figure S1: Reversing, oscillatory flow in the AVC between 36 and 48 hpf. A-C) Maximum projection of the three-dimensional reconstruction of a 36 hpf *Tg(fli:kaede;gata1:dsRed)* zebrafish heart at three different instants of the heart beat. The dsred labelled red blood cells are shown in magenta, while endocardial cells are shown in green. D,E) Flow direction in the AVC at D) 36hpf and E) between 36-48 hpf: magenta, flow moves from atrium to ventricle; black, flow is from ventricle to atrium; white, no flow or not visible. F) Average percentage of reversing flow per heart beat. G-I) Computational model for RBC flows between 36-48 hpf at three different instants of the heart beat (cf. Movie 1). J) Flow direction in the AVC model: solid arrows point in the direction of the flow. Dashed squares point out the uneven-time dependent distribution of RBCs in K) the model, and L,M) in vivo.

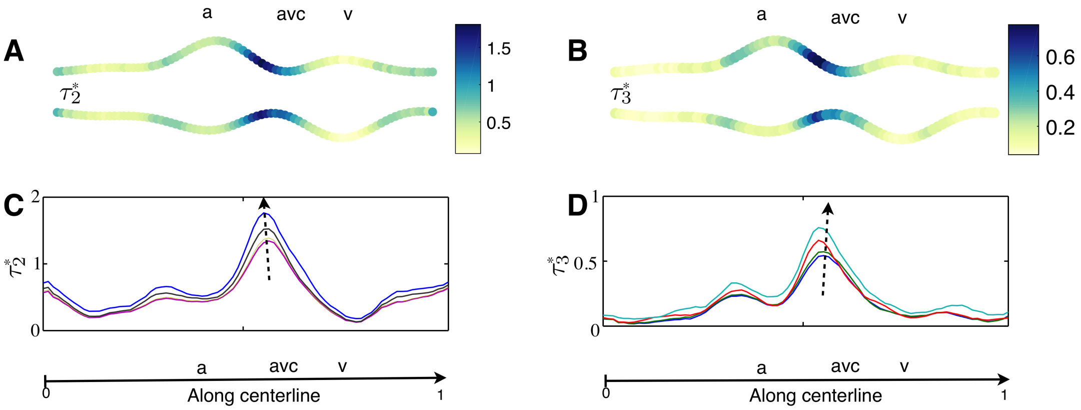

Figure S2: Shear stress pattern during tissue convergence (higher harmonics) in complement to Fig. 3. A,C) Second ($\tau_2$) and B,D) third ($\tau_3$) harmonics. The results in A and B are for 106 red blood cells. The results on C and D are for the upper wall and for different numbers of red blood cells $n_p$ =1, 17, 54,106 (arrows point to larger values of $n_p$). The superscript $^*$ denotes that results are normalized by the space average of $\int_t f_1|\tau|dt$. a: atrium; avc: atrioventricular canal; v: ventricle.

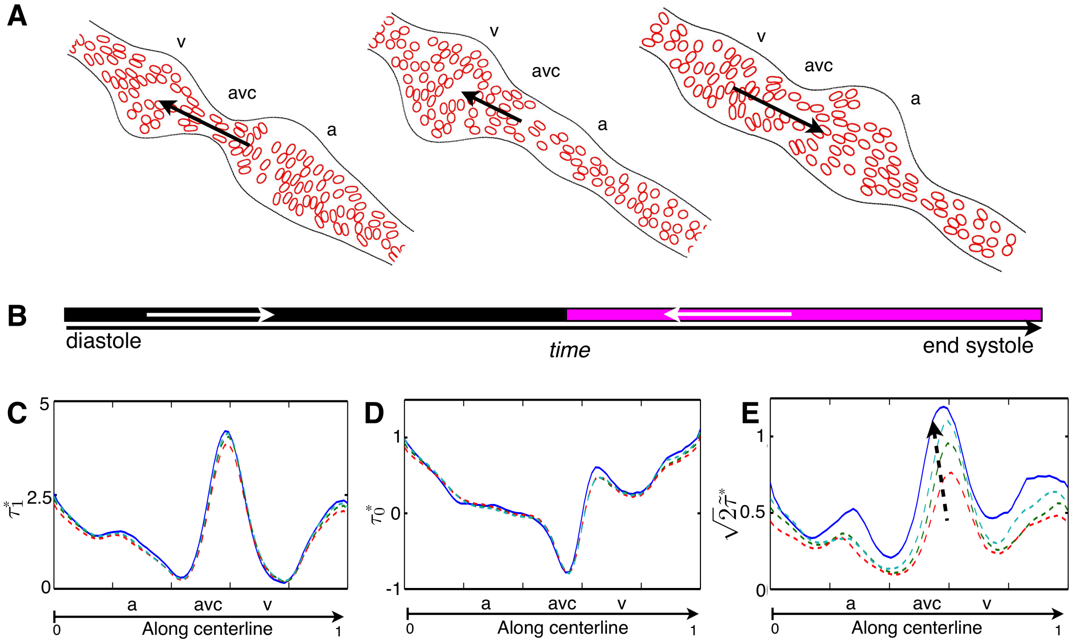

Figure S3: Model sensitivity to red blood cell (RBC) shape and stiffness. Related to Fig. 3. A) Computational model for RBC flows at three different instants of the heart beat for round elastic red blood cells (cf. Fig. S1G-I). B) Flow direction in the AVC model: magenta, flow is from atrium to ventricle; black, flow is from ventricle to atrium; white, no flow or not visible. Solid arrows point in the direction of the flow. C) Fundamental harmonic $\tau_1$, D) time average $\tau_0$, and E) non-periodic oscillation $\tilde{\tau}$ of the shear stress. C-E) The blue solid line corresponds to the RBC shape of the test case of Fig. S1 and 3, $n_p$ =106, and $\tau_{rlx}/\tau_U = 0.16$. The three dashed lines correspond to the rounder RBC shape shown in A and are obtained using the same, stiffer ($\tau_{rlx}/\tau_U = 0.1$), and softer ($\tau_{rlx}/\tau_U = 0.32$) RBC membranes (dashed arrow points to larger value of stiffness). The superscript $^*$ denotes that results are normalized by the space average of $\int_t f_1|\tau|dt$. a: atrium; avc: atrioventricular canal; v: ventricle.